https://doi.org/10.5194/egusphere-2026-422
Preprint. Discussion started: 4 February 2026

A Novel Synergistic Approach Using Altimeter Backscatter for an Improved Radiometer Thin Sea Ice Thickness Retrieval

Ferran Hernández-Macià[1,2,3], Maria José Escorihuela[2], Carolina Gabarró[1], Gemma Sanjuan Gomez[3], and Albert Garcia-Mondéjar[2]

[1]Barcelona Polar Lab (BPL), Institute of Marine Sciences (ICM-CSIC), Barcelona, Spain
[2]isardSAT, S.L., Barcelona, Spain
[3]Autonomous University of Barcelona (UAB), Cerdanyola del Vallès, Spain

Correspondence: Ferran Hernández-Macià (fhernandezmacia@icm.csic.es)

Abstract. This study proposes a novel altimetry-radiometry synergistic approach for improving SMOS thin sea ice thickness retrievals by incorporating permittivity estimates derived from CryoSat-2 backscatter observations. Since sea ice permittivity remains the dominant source of uncertainty in L-band radiometric thickness retrievals, the sensitivity of the CryoSat-2 backscatter signal to variations in this parameter offers a promising pathway to better constrain it. By integrating these permittivity estimates into a hybrid scheme that includes the inversion of an L-band sea ice emission model using machine learning, the approach aims to enhance the accuracy and robustness of thin sea ice thickness estimates obtained from SMOS. A set of independent in situ datasets is used to validate the proposed methodology and to assess its performance across different ice regimes. The CryoSat-2-derived permittivity values lead to realistic and physically consistent estimates, although its validity is limited to first-year ice. Overall, the synergistic combination of Ku-band altimetry and L-band radiometry yields improved results compared to SMOS-only retrieval methods, which are included as a baseline for reference. This highlights the potential of cross-sensor synergies to advance thin sea ice monitoring, establishing a framework applicable to present and future satellite missions such as CIMR, CRISTAL, and ROSE-L.

1 Introduction

Sea ice is a critical component of the Arctic climate system, influencing energy exchange, ocean circulation, and weather patterns (Meredith et al., 2019). It also serves as a key indicator of climate change, with its thickness and extent closely monitored using satellite remote sensing. Passive microwave radiometry has served for polar monitoring since the 1970s, with the first satellites being capable of retrieving sea ice concentration (SIC). The launch of European Space Agency (ESA)'s Soil Moisture and Ocean Salinity (SMOS, Kerr et al. (2010)) and National Aeronautics and Space Administration (NASA)'s Soil Moisture Active Passive (SMAP; Entekhabi et al. (2010)) missions, which operate at L-band (1.4 GHz), enabled the retrieval of sea ice thickness (SIT) for thin ice regimes ($\leq$ 1 m; Kaleschke et al. (2012), Maass et al. (2015)). Furthermore, the upcoming Copernicus Imaging Microwave Radiometer (CIMR) will extend these capabilities by integrating L-band with C-, X-, K-, and Ka-band channels (1.41, 6.90, 10.65, 18.70 and 36.50 GHz, respectively), thus providing simultaneous continuity of both sea ice concentration and thickness measurements (Donlon et al., 2023). Complementarily, satellite altimeters such as the current

https://doi.org/10.5194/egusphere-2026-422
Preprint. Discussion started: 4 February 2026

sensors on ESA's CryoSat-2 (Laxon et al., 2013) and NASA's ICESat-2 (Markus et al., 2017), are sensitive to thicker ice (> 1 m). These satellites measure sea ice freeboard, which can be converted to total thickness under hydrostatic equilibrium assumptions. However, this conversion remains sensitive to estimates of snow depth and density, and also ice density, which are major sources of uncertainty (Warren et al. (1999), Mallett et al. (2021)). A combined SMOS and CryoSat-2 thickness product exists (Ricker et al., 2017), offering full thickness coverage, but it inherits the individual limitations of both SMOS and CryoSat-2 retrievals.

Nowadays, two SMOS-based thin sea ice thickness operational products exist for the non-melting period (October–April). The first, ESA's official product developed by the Alfred Wegener Institute (AWI), uses a semi-empirical algorithm that does not account for snow cover, despite snow significantly affecting L-band radiation (Tian-Kunze et al., 2014). The second, from the University of Bremen (UB), is an empirical product but has a limited sensitivity range, reaching only up to approximately 0.5 m (Huntemann et al., 2014). Recent efforts to enhance the retrieval have employed machine and deep learning methodologies (Hernández-Macià et al. (2024a), Hernández-Macià et al. (2025)). Despite some improve in the accuracy and a reduction in the required computational resources, these approaches did not lead to a groundbreaking advance. Therefore, these limitations highlight the need for improved retrieval methods that can enhance accuracy and extend the sensitivity of SMOS-based ice thickness estimates.

All these SMOS-based thin sea ice thickness retrieval methods rely on emission modeling, and therefore, the knowledge of the sea ice permittivity is required, while it is a parameter that remains poorly constrained due to the complex composition of the sea ice (Huntemann (2015), Hernández-Macià et al. (2024b)). Theoretical models represent sea ice as a matrix containing brine inclusions of different geometries (e.g., spheres, needles; Shokr (1998)) that depend on ice growth conditions. However, no direct method exists to infer permittivity from satellite measurements, and the limited current knowledge of the modeled permittivity introduces uncertainties in thickness retrievals. Hereafter, the terms permittivity and dielectric constant are used interchangeably, as both usually appear in the literature with the same meaning.

Previous works have studied the physical dependencies of the so-called backscatter measured by CryoSat-2 (Dawson and Landy, 2023). By definition, the measured backscatter is a function of various parameters of the satellite, but also of different physical properties of the media where the reflection of the signal happens. To estimate the sea ice permittivity at L-band, a relation with the backscatter measured at CryoSat-2's Ku-band can be established. Physically, the backscatter signal represents the fraction of the energy that is scattered back toward the satellite by the snow-covered sea ice. Its magnitude depends strongly on the dielectric contrast of the medium, i.e. on the interface, where the reflection happens, as well as on its surface roughness. Despite previous efforts (Landy et al., 2020), remains difficult to determine and distinguish the impact of these two variables on the scattered signal. In fact, Grenfell et al. (1998) showed that nadir radar returns are primarily a function of effective permittivity, modulated by surface roughness and internal inhomogeneities. However, this study is founded on the assumption that the reflection happens in the snow-ice interface, and thus the observed backscatter is highly dependent on the refraction index contrast of these two media, and so of the permittivity of the sea ice. Therefore, one can use this dependence to obtain

https://doi.org/10.5194/egusphere-2026-422
Preprint. Discussion started: 4 February 2026

information about the sea ice permittivity.

This study proposes a cross-sensor synergy that operates at a more fundamental level compared to the standard merging of final products to extend spatial or temporal ranges. The synergy is exploited at an earlier stage, exploring the observational sensitivity of one satellite to constrain the physical retrieval parameters relevant for the other. Specifically, sea ice permittivity estimates derived from CryoSat-2 backscatter are incorporated into the L-band microwave emission model. By integrating this constrained variable into the retrieval chain, it is aimed to refine the accuracy of thin sea ice thickness estimates obtained from SMOS observations.

The paper is organized as follows: Section 2 details the data sources used within the methodology, and the in situ datasets used for validation. Section 4 describes the proposed retrieval methodology. Section 5 presents the results of the study, which are then in Section 6. Finally, Section 7 summarizes the main findings and conclusions.

2 Data

2.1 SMOS brightness temperature

The SMOS satellite carries the Microwave Imaging Radiometer Aperture Synthesis (MIRAS), a passive L-band radiometer that records full-polarization brightness temperatures (TB) and the four Stokes parameters across incidence angles spanning 0° to 60° (Kerr et al., 2001). The sensor provides full polar coverage on a daily basis, with a global revisit time of three days. MIRAS generates 2D interferometric snapshots with a swath width of approximately 1200 km and a temporal resolution of 1.2 s. Depending on the incidence angle, the spatial resolution varies from $\sim$35 km at nadir to over 50 km at the swath edges. The instrument directly measures horizontally (TBH) and vertically (TBV) polarized TBs in the antenna reference frame, from which the total intensity is calculated as the average of the two components. Given that the L-band intensity signal over sea ice remains almost constant at lower incidence angles, the measurements acquired between 0° and 40° are averaged. Finally, daily Arctic brightness temperature intensities are interpolated using a nearest-neighbor approach and mapped to the NSIDC polar stereographic projection with 12.5 km grid spacing

In this study, the TB is extracted from the Alfred Wegener Institute (AWI)/European Space Agency (ESA) L3 Sea Ice Thickness product. This product provides Arctic sea ice thickness (SIT) estimates from October to April, covering the period 2010–present (Tian-Kunze et al., 2014). This choice ensures consistency, as all datasets used in the methodology are regridded to this product's grid. Moreover, its SIT estimates are included in the results as a baseline. This product, called AWI/ESA hereafter, relies on an iterative inversion scheme coupling a thermodynamic ice growth model with a three-layer radiative transfer model, comprising sea ice and ocean components while neglecting snow cover. The forward model simulates the medium emissivity, which is further used to estimate the TB. The bulk ice temperature is derived from 2 m air temperatures provided by atmospheric reanalysis. Bulk salinity is parameterized using the empirical function described by Ryvlin (1974). Ultimately, to account for sub-pixel heterogeneity within the radiometer's footprint, the algorithm integrates a statistical thickness distribution function calibrated against Operation IceBridge (OIB) airborne data.

https://doi.org/10.5194/egusphere-2026-422
Preprint. Discussion started: 4 February 2026

2.2 CryoSat-2 Ku-band backscatter

CryoSat-2 (hereafter CS2) is equipped with the Synthetic Aperture Interferometric Radar Altimeter (SIRAL), a Ku-band radar altimeter (13.575 GHz) optimized for sea ice and polar observations. In SAR and SARIn modes, Doppler beam sharpening improves the along-track resolution up to ∼300 m while the across track is limited by the antenna footprint to ∼1.5 km. In this work, the CS2 Level-2 Baseline E data products are used, which include radar backscatter measurements derived from SAR mode acquisitions over sea ice. These data have already undergone calibration and instrument corrections through the ESA processing chain. Processing detail can be found in the CS2 Product Handbook (ESA, 2021).

The backscatter data are averaged within a 15 day window and regridded onto the 12.5 km NSIDC polar stereographic grid to allow its inclusion in the algorithm's workflow. This accounts for the spatial resolution mismatch between the two satellites, limiting gaps in the backscatter maps while retaining sensitivity to variations.

For a spaceborne Ku-band radar altimeter such as CryoSat-2, the sea ice backscatter is dominated by surface, or interface, scattering (Beaven et al., 1995). This contribution arises at dielectric discontinuities, thus at the snow-ice interface. Therefore, the volume scattering contribution can be safely neglected. Following Fetterer et al. (1992) and Tonboe (2017), the backscatter at nadir is:

$$\sigma^0 = 0.9F|R(0)|^2 \frac{H}{u\tau}, \tag{1}$$

where $|R(0)|$ is the Fresnel reflection coefficient at nadir, F is the fraction of the flat-patch area (unitless, inversely proportional to the roughness), H is the satellite height, u the pulse propagation speed, and τ the pulse length. Therefore, in general, this backscatter is a function of the reflection coefficient, which depends on the dielectric contrast of the snow-ice interface, and the surface roughness. Note that this assumption may not hold over fresh lake ice, where Ku-band penetration often leads to double-peak waveforms reflecting from both the snow-ice and ice-water interfaces (Mangilli et al., 2024).

2.3 Ice surface temperature satellite product

Daily surface thermal fields are obtained from the Arctic Ocean-Sea and Ice Surface Temperature Reprocessed dataset (Copernicus Marine Service (CMEMS), 2024a), produced by the Danish Meteorological Institute (DMI) and available through the Copernicus Marine Service (CMEMS). This record aggregates reprocessed thermal infrared data from different sensors, including the Advanced Very High Resolution Radiometer (AVHRR), the Advanced Along Track Scanning Radiometer (AATSR), and the Sea and Land Surface Temperature Radiometer (SLSTR). These inputs are extracted from the ESA Climate Change Initiative (CCI), the Copernicus Climate Change Service (C3S), and the Arctic & Antarctic Ice Surface Temperatures from Thermal Infrared Satellite Sensors (AASTI) dataset. Provided on a $0.05°$ grid covering the open ocean, marginal ice zone, and packed ice, the product employs an optimal interpolation method that utilizes the previous day's analysis as the background field.

https://doi.org/10.5194/egusphere-2026-422
Preprint. Discussion started: 4 February 2026

In this study, a linear temperature profile within the ice is considered, following the approach of Huntemann (2015). Under this assumption, the bulk ice temperature (T_{ice}) is expressed as

$$T_{ice} = \frac{T_{surface} - T_{sw}}{2}, \tag{2}$$

where $T_{surface}$ is the satellite-derived surface temperature, and T_{sw} represents the seawater temperature, set to a typical Arctic value of $-1.8°\mathrm{C}$.

2.4 Arctic Ocean Physics Reanalysis

Auxiliary ocean and sea ice variables are extracted from the Arctic Ocean Physics Reanalysis, a product generated by the Nansen Environmental and Remote Sensing Center (NERSC) and distributed by CMEMS (Copernicus Marine Service (CMEMS), 2024b). This reanalysis model is based on TOPAZ4b, which assimilates diverse observational datasets to constrain the model state. Assimilated data sources include sea level anomalies from satellite altimetry, sea surface temperature from the Operational Sea Surface Temperature and Sea Ice Analysis (OSTIA), OSI-SAF sea ice concentration, CS2SMOS sea ice thickness fields, sea surface salinity from the Barcelona Expert Center (BEC) SMOS product, and in situ temperature and salinity profiles from moorings and cruises.

For this study, sea ice thickness, seawater salinity, and snow depth are extracted from this reanalysis. The bulk sea ice salinity is estimated using the empirical relation proposed by Ryvlin (1974):

$$S_{ice} = S_{sw}(1 - S_R)e^{-a\sqrt{d_{ice}}} + S_R S_{sw}, \tag{3}$$

where S_{sw} is the seawater salinity and d_{ice} is the sea ice thickness (in cm), both taken from the reanalysis product. The growth rate coefficient is a, which typically ranges from 0.35 to 0.5, and S_R corresponds to the residual bulk salinity at the end of the growth season. While the original formulation by Ryvlin (1974) proposed $a = 0.5$ and $S_R = 0.13$, the adjusted parameterization from Kovacs et al. (1996) is used in this work, setting $S_R = 0.175$ to improve consistency with Arctic field observations.

Snow presence is derived directly from the reanalysis snow thickness variable: a positive thickness indicates snow cover, whereas a value of zero implies no snow.

2.5 In situ datasets

The in situ validation datasets consist of measurements collected by moored instruments at two Arctic Ocean sites, complemented with observations from a 2014's field campaign in the Barents Sea, where unusually thin sea ice was encountered for that season. For all the datasets presented, it is important to note that each in situ measurement corresponds to a single point within much larger satellite pixels, and therefore substantial representation errors and biases are unavoidable. Nevertheless, the validation procedure is applied consistently across all compared products, ensuring that the effects of this resolution mismatch influence them in an equivalent manner to all SIT datasets.

https://doi.org/10.5194/egusphere-2026-422
Preprint. Discussion started: 4 February 2026

2.5.1 ESA SMOSice Campaign data

Part of the validation is performed using data from the ESA SMOSice campaign, which measured thin ice regimes southeast of Svalbard, in the Barents Sea, during March 2014 (Kaleschke et al., 2016). The campaign involved coordinated acquisitions from the RV Lance and the Polar 5 research aircraft. Electromagnetic induction (EM) sounders were deployed on both platforms: a ship-based system (SEM) mounted on the vessel's bow and an airborne system (HEM) suspended from a helicopter. Additionally, the Polar 5 aircraft carried a Riegl VQ-580 airborne laser scanner (ALS) to measure freeboard, which was subsequently converted to thickness assuming hydrostatic equilibrium. All datasets were subsequently interpolated to the 12.5 km grid of the AWI/ESA SMOS sea ice thickness product using arithmetic averaging with the GMT blockmean tool (Wessel et al., 2019), as provided by Dr. Lars Kaleschke. This dataset was also used to validate the ESA's official SMOS sea ice thickness product (Kaleschke et al., 2016).

2.5.2 Shipborne Sea Ice Monitoring System (SIMS) data

The Sea Ice Monitoring System (SIMS) is an instrument mounted onboard the Le Commandant Charcot ship from the PONANT company. It is located in the front of the ship and it consists of two components, namely a sonar measuring the distance to the air-snow interface and an EM31 measuring the distance to the ice-water interface (von Abedyll and Haas, 2024). It measures the total thickness (snow + sea ice), so a bias has to be expected when comparing to satellite-based SIT retrievals. Given its nature, it allows to continuously monitor the thickness while navigating through the ice, delivering highly valuable dataset for validating remote sensing products. Particularly, the data used in this study was collected from the 29th of March to the 15th of April of 2025, in the west coast of Greenland. Specifically, it consists of measurements from two legs that navigated in Baffin Bay and along the coast, from approximately 66ºN 53ºW to 74ºN 57ºW.

2.5.3 BGEP moorings data

The Upward-Looking Sonar (ULS) instruments deployed on moorings as part of the Beaufort Gyre Exploration Project (BGEP) provide measurements of sea ice draft, i.e., the submerged portion of the ice. Since the ULS measures ice draft rather than total thickness, a conversion step is required. A multiplicative scaling factor of 1.136 is applied to the draft, following the approach validated by Belter et al. (2020). This coefficient is based on an empirical analysis of approximately 400 drill-hole measurements collected in the Fram Strait (Vinje and Finnekåsa, 1986). The BGEP dataset, used here for validation, consists of the daily mean sea ice thickness values from three ULS moorings (A, B, and D) located within the Beaufort Gyre.

3 Sea ice permittivity modeling

The permittivity of the media is a key parameter of its emission modeling. It can be defined in a complex formulation:

$$\epsilon = \epsilon' - i\epsilon'' \tag{4}$$

https://doi.org/10.5194/egusphere-2026-422
Preprint. Discussion started: 4 February 2026

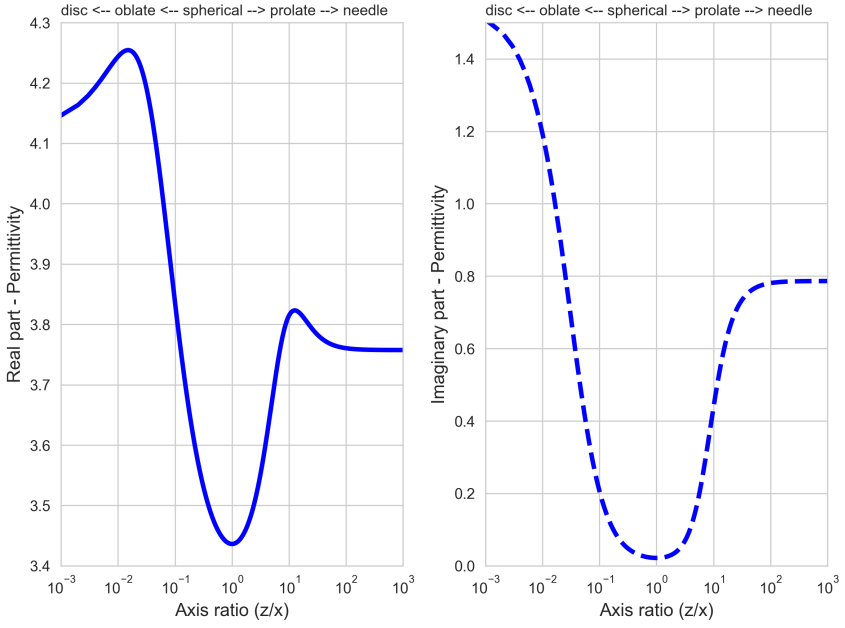

Figure 1. Sea ice permittivity at L-band frequency (1.4 GHz) as a function of the axis ratio of the brine inclusions, modeled as randomly-oriented ellipsoids (from Polder-van Santen model). The axis ratio (z/x) correspond to the ratio between the vertical (z) and horizontal (x) axes of the ellipsoid.

where ϵ' is the real part, and ϵ'' is the imaginary part. In qualitative terms, the real part determines the extent to which energy can penetrate a material, whereas the imaginary part corresponds to the loss, i.e. the amount of energy dissipated within the material. Higher ϵ' indicates less penetration, whereas higher ϵ'' denotes more energy dissipation.

Sea ice can be modeled as an heterogeneous mixture of pure ice, liquid brine inclusions, and air pockets (Ulaby et al., 2014). These brine inclusions strongly affect the permittivity of the media, given the high contrast with the pure ice. The conditions and the rate in which the sea ice grows play a role on the shape and orientation of the brine inclusions, but this information is usually not known. In general, harsh conditions during formation are linked to randomly oriented needle-like inclusions, while calmer conditions with low temperature fluctuations are related to spherical inclusions or vertically oriented needles or ellipsoids (Vant et al. (1978), Shokr (1998)). Furthermore, it is also a function of the brine volume, which ultimately depends on the temperature and salinity of the ice (Assur (1960), Frankenstein and Garner (1967)).

Figure 1 shows the sea ice permittivity, both real and imaginary parts, at L-band as a function of the shape of the brine inclusions. The permittivity is computed using the Polder-van Santen model, assuming that the brine inclusions are randomly-oriented ellipsoids with a certain axis ratio (Jones and Friedman, 2000), and with a fixed temperature and salinity of -10^oC and 5, respectively.

In microwave remote sensing of sea ice, the relevance of the complex permittivity components varies by application. The real part is typically more relevant in altimetry, as it governs not only the surface reflection coefficient but also the propagation

https://doi.org/10.5194/egusphere-2026-422
Preprint. Discussion started: 4 February 2026

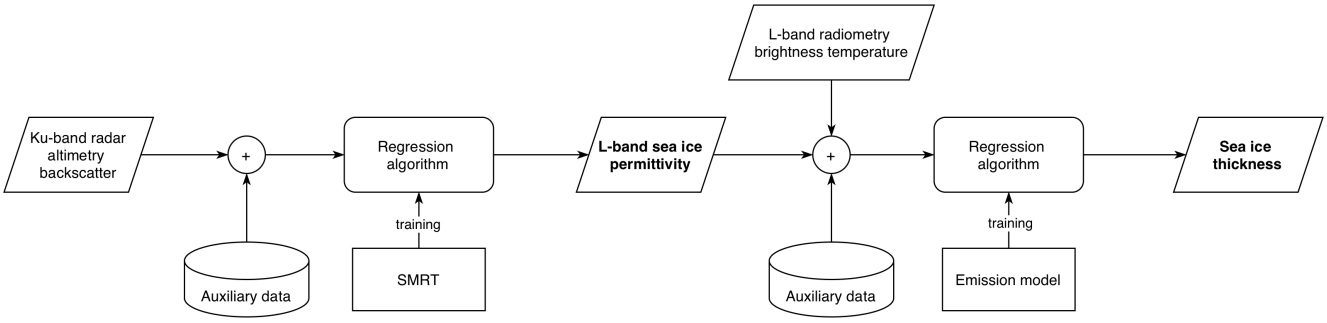

Figure 2. Conceptual workflow of the proposed synergistic methodology. The retrieval is performed in a cascade: first, CryoSat-2 backscatter constrains the sea ice permittivity (RF-eps); second, this permittivity informs the inversion of SMOS brightness temperatures to retrieve sea ice thickness (RF-sit).

velocity, a critical factor for correcting range biases in penetrating radar signals. Conversely, the imaginary part is often the primary driver in radiometry, as it dictates the dielectric loss and penetration depth, thereby defining the effective emission layer. However, ϵ' also influences significantly the radiometric brightness temperatures by determining the impedance mismatch and transmissivity at the interfaces. In fact, both components are intrinsically coupled, since they are both derived from the same brine inclusions configurations and the same brine volume fraction, i.e. temperature and salinity conditions. In this work, the focus is specifically the First-Year Ice (FYI), as the study and the method proposed addresses thin ice regimes only.

4 Methodology

This study proposes a synergistic methodology to retrieve thin SIT by combining active and passive microwave observations. This is done with a two-stage hybrid inversion scheme that utilizes Ku-band radar altimeter backscatter to constrain the dielectric properties of sea ice prior to inverting L-band TBs. The workflow, summarized in Figure 2, is composed of two sequential steps. First, CS2 backscatter is used to estimate the sea ice permittivity. This is achieved through a hybrid scheme where the Snow Microwave Radiative Transfer (SMRT) model simulates the link between surface scattering and dielectric properties to train the regression algorithm. Secondly, the CS2-derived permittivity estimates are combined with SMOS TB observations. These inputs are fed into a second hybrid retrieval algorithm that estimates thin SIT. The methodology is detailed in the following subsections. Section 4.1 describes the generation of the synthetic training dataset using the SMRT model, which establishes the link between Ku-band backscatter and sea ice permittivity. Section 4.2 outlines the application of the trained regression model with CS2 observations. Finally, Section 4.3 presents the synergistic retrieval framework, explaining how the CS2-estimated permittivity is combined with SMOS TB (and auxiliary inputs) to retrieve SIT.

https://doi.org/10.5194/egusphere-2026-422
Preprint. Discussion started: 4 February 2026

4.1 SMRT simulations: linking backscatter and permittivity

To generate the training dataset for estimating the sea ice permittivity from the radar backscatter, the SMRT model is used in the altimetry set up (validated in Larue et al. (2021)). The forward model is configured with the CryoSat-2 sensor geometry, using the `nadir_lrm_altimetry` module. Surface and interface roughness is modeled with a Geometrical Optics (GO) rough interface, assuming a Mean Square Slope (MSS) of 0.03 m for both the air-snow and the snow-ice interfaces (based on Landy et al. (2020) and Larue et al. (2021)). The simulated medium consists of a snow-covered ice column. The snowpack is parameterized as a single exponential layer of 0.1 m thickness, density of 300 kg m^{-3}, correlation length of 5×10^{-5} m, and fixed temperature (268 K) with no salinity. Below the snowpack, a first-year sea ice layer of 1 m thickness is included. The ice microstructure follows the independent-sphere model with radius 1 mm, density of 900 kg m^{-3}, and variable bulk salinity. To account for non-spherical inclusions, the Polder-Van Santen mixing formula (modified to include randomly oriented ellipsoids) is used to compute the complex permittivity as a function of brine inclusion axis ratio, temperature, and salinity. Simulations are carried out across a parameter space of sea ice temperature (255-270 K, step 0.5 K), sea ice salinity (3-10, step 0.5), and a wide range of ellipsoidal axis ratios (10^{-3}–10^{3}). For each configuration, the model computes the backscatter coefficient (σ^0) in dB. Specifically, the simulated backscatter is defined as the maximum of the simulated waveform. This formulation is consistent with Larue et al. (2021), who compute the backscatter coefficient via the echo amplitude following Wingham et al. (1986), a parameter that is largely governed by the peak power. Furthermore, sensitivity tests conducted within this framework have confirmed an equivalence between the waveform maximum and the computed amplitude.

A sensitivity analysis can be performed to showcase which roles are the permittivity and the roughness (determined by the MSS) playing in the simulated backscatter. Figure 3 shows the simulated CS2 backscatter as a function of the axis ratio of the brine inclusions of the sea ice, ranging from a disc (left), through and sphere, and to a needle (right). The simulation is run for different roughness parameterizations, with values for the MSS ranging from $1e-05$ to 1 m. SMRT is run with the GO approximation for both interfaces, as done in Larue et al. (2021). This roughness model is valid for MSS similar or larger than the wavelength of the sensor, i.e. 2.3 cm for the Ku-band. Figure 3 contains the simulations within a reasonable valid range at the CS2 frequency. As shown, variations in surface roughness primarily affect the absolute magnitude of the simulated backscatter, while the spread between the maximum and minimum values changes only marginally.

A notable outcome is that the simulated CS2 backscatter values are negative, whereas the distributed CS2 products typically exhibit positive values of similar magnitude. This discrepancy arises because the satellite backscatter coefficients are calibrated using system-specific reference constants that are not available to be included in the simulations (Dinardo, 2016). However, this absolute offset does not impact the validity of the proposed method. Since the analysis relies on the relative variations and statistical correlation of the signal rather than on the values accuracy, the simulation results remain robust. Crucially, the dynamic range of the simulations mirrors that of the observations, ensuring that the distribution of backscatter differences remains consistent with satellite data.

https://doi.org/10.5194/egusphere-2026-422
Preprint. Discussion started: 4 February 2026

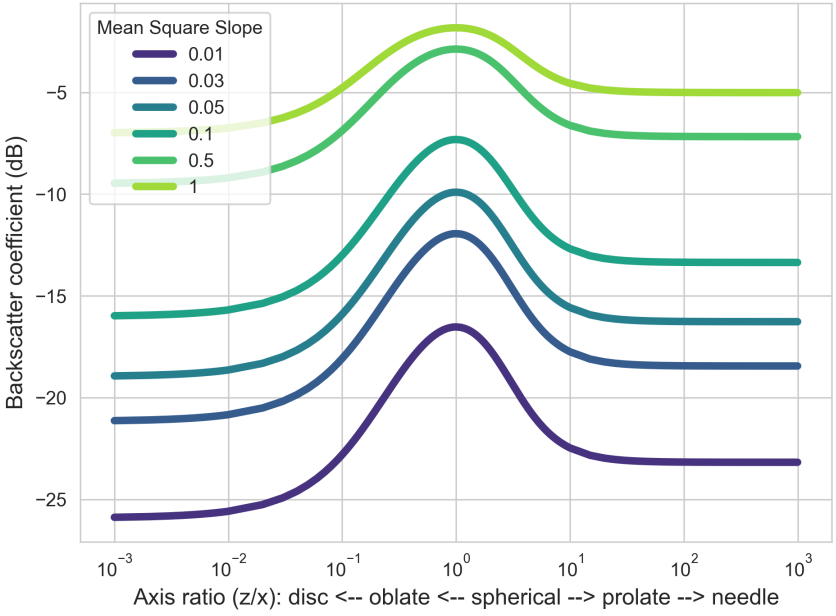

Figure 3. CryoSat-2 backscatter simulated with SMRT as a function of the axis ratio of the brine inclusions of the sea ice. The output is showed for different Mean Square Slope (MSS) values, i.e. for different roughness'. All the other parameters are fixed and constant along the different simulations. The axis ratio (z/x) correspond to the ratio between the vertical (z) and horizontal (x) axes of the ellipsoid.

Prior to training, the dataset is scaled using a *Standard Scaler*, which standardizes it by removing the mean and scaling to unit variance:

$$x' = \frac{x - \mu}{\sigma}, \tag{5}$$

where x is the original feature value, μ is the mean of the feature, and σ its standard deviation. This is done to ensure consistency with Figure 3, which indicates that the relative range of backscatter as a function of the axis ratio is largely preserved for the different roughness cases, as stated before. Therefore, the scaling is applied to use the backscatter differences across the axis ratio range, rather than the absolute simulated backscatter values.

In parallel, the permittivity of the sea ice is computed after the Polder-van Santen dielectric mixing model (see Section 3), using the same axis ratio, temperature and salinity that are used to run the SMRT simulation. The resulting dataset links σ^0 with the real and imaginary parts of the permittivity, as well as the physical drivers (sea ice temperature and salinity). Figure 4 shows the simulated Ku-band backscatter (already scaled) as a function of the real and imaginary parts of the sea ice L-band permittivity for the range of temperature and salinity conditions. It is important to remark that this relation is obtained from the simulations, so its reliability lies in the robustness of the used models. Therefore, it is not claimed that this relation is valid in any circumstance, and the proposed method relies on the statistical relation, which is further learned by the machine learning algorithm.

https://doi.org/10.5194/egusphere-2026-422
Preprint. Discussion started: 4 February 2026

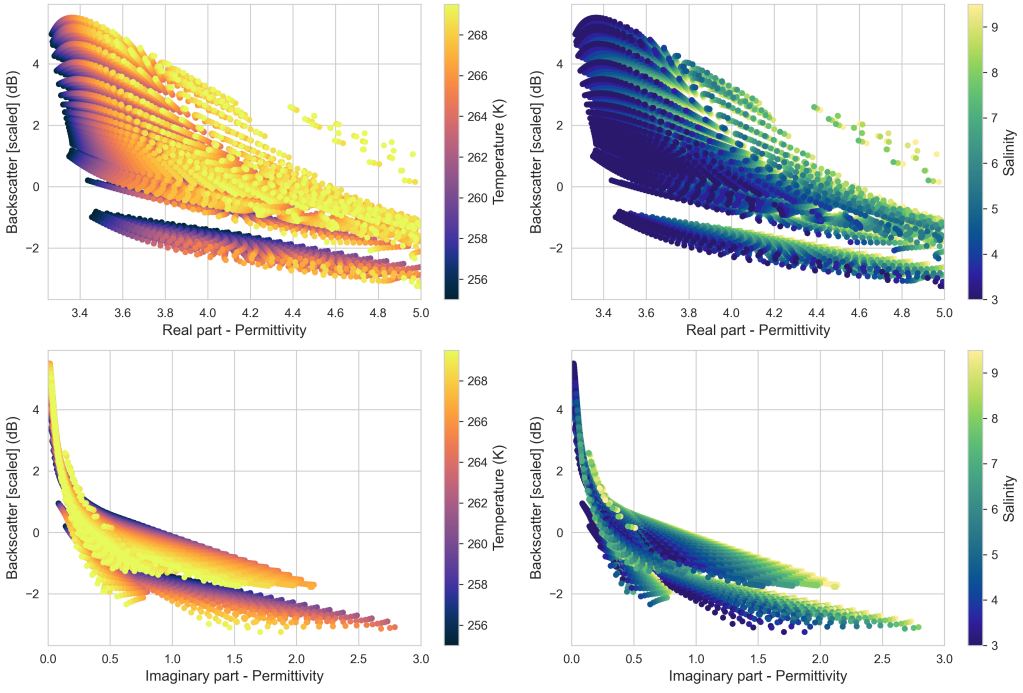

Figure 4. Simulated Ku-band backscatter (scaled) as a function of the real (upper) and imaginary (lower) parts of the L-band sea ice permittivity. The colormaps show the temperature (left) and salinity (right) for each simulated estimation.

This generated dataset can then be used to train a Random Forest (RF) regression model, hereafter called RF-eps (as 'eps' makes reference to ϵ, used to depict the permittivity of a media). Since RF-eps is based on a decision tree algorithm, it enables the interpretation of predicted results by analyzing the feature importance: backscatter dominates (89%), followed by salinity (6%) and temperature (5%).

4.2 Estimating permittivity using CryoSat-2 backscatter

After the RF-eps algorithm being trained with the dataset generated through SMRT model-based simulations, permittivity estimations can be done from CS2 data. To do so, biweekly CS2 data (see Section 2.2) is interpolated to the 12.5 km x 12.5 km NSIDC Polar Stereographic grid, which is the one used for the SMOS product. Prior to be used as input for the RF-eps algorithm, the biweekly CS2 backscatter maps are denoised using a bilateral filter (Tomasi and Manduchi, 1998), which performs edge-preserving smoothing by combining a spatial kernel with an intensity kernel. In practice, each grid cell is replaced by a weighted average of its neighbors, where the weights decrease with both geographical distance and backscatter difference, thus reducing small-scale noise while maintaining sharp spatial gradients in the signal. Figure 5 shows the workflow of the training and prediction stages for the RF-eps algorithm. In the training step, the temperature, salinity and axis ratio conditions are taken from the ranges detailed in Section 4.2, and used to simulate the backscatter and the permittivity in

https://doi.org/10.5194/egusphere-2026-422
Preprint. Discussion started: 4 February 2026

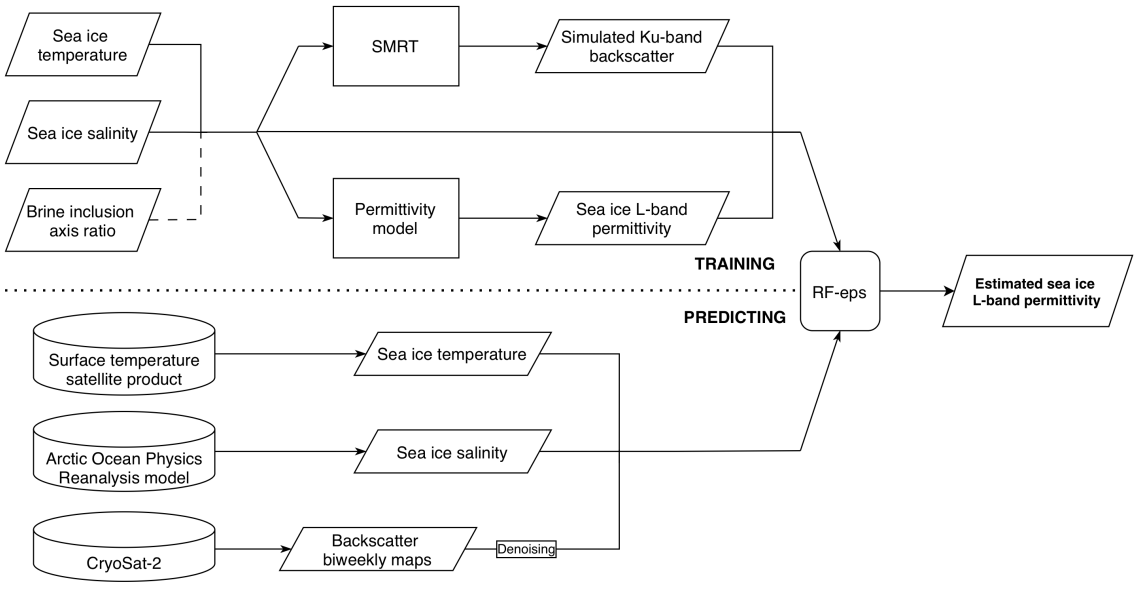

Figure 5. Diagram summarizing the training and predicting workflows of the RF-eps algorithm.

parallel. It is worth mentioning that, even though the brine inclusion axis ratio is used to simulate both the Ku-band backscatter with SMRT and the L-band sea ice permittivity with the formulation presented in Section 3, it is not included as a input in the RF-eps algorithm (dashed line in 5). This is because this variable is normally not known at the satellite scales, and even less for pan-Arctic applications. When computing the L-band sea ice permittivity estimations, the sea ice temperature and salinity are obtained from the same sources as for the SMOS-only thin sea ice thickness retrieval (Hernández-Macià et al. (2024a), Hernández-Macià et al. (2025)), and also for the informed retrieval presented in the next Section 4.3.

4.3 Integrating altimetry-derived permittivity into SMOS thin sea ice thickness retrieval

Once the permittivity estimates have been retrieved from the CS2 backscatter observations, this information is used as input to retrieve the thin SIT from SMOS TB measurements. This second part of the methodology has been described in detail in previous works, such as Hernández-Macià et al. (2024a) and Hernández-Macià et al. (2025). However, in this study it is slightly modified to include the sea ice permittivity as input. In the original method, the sea ice permittivity was only a function of the bulk temperature and salinity, using the Vant empirical formulation (Vant et al., 1978). In this improved methodology, the permittivity is derived from CS2 backscatter observations using the RF-eps algorithm (described in Section 4.2), which follows the theoretical framework of Shokr (1998). The key advancement lies in accounting for a permittivity that depends not only on sea-ice temperature and salinity, but also on the ellipsoidal shape of the brine inclusions.

Similarly to what is done to train RF-eps, and due to the lack of in situ data available in the Arctic, a training dataset is generated through a model-based simulation to train a RF algorithm. Specifically, the Burke formulation (Burke et al., 1979) is

https://doi.org/10.5194/egusphere-2026-422
Preprint. Discussion started: 4 February 2026

selected as radiative transfer model. This model relies on a set of simplifying assumptions. Radiation is treated within an energy conservation framework (i.e., incoherently), with no emission or attenuation considered along the propagation path between the surface and the sensor. The atmosphere is represented by an isotropic sky brightness temperature of 5 K. Each layer is assumed to be homogeneous, characterized by constant permittivity, temperature, and salinity, and the interface is treated as smooth. Under these conditions, the observed brightness temperature results from the superposition of the emission from the layered medium and the fraction of the sky radiation reflected at the surface. Since the model represents the medium as a stratified system, four layers are considered in this approach: air – snow – ice – water, with the uppermost (air) and lowermost (ocean) layers treated as semi-infinite, assuming for the latter typical Arctic conditions of –1.8°C temperature and a salinity of 33. The overlying snow is assumed to be isothermal with the underlying ice, non-saline, and to have a thickness equal to 10% of the ice thickness, following the formulation of Doronin (1971). Previous work (Maass et al., 2015) has shown that, at L-band, the satellite-observed brightness temperature is sensitive only to the presence of snow and not to its amount, allowing the effect of varying snow depth to be neglected.

The reliability of the simulation depends on the accuracy of L-band sea ice emission modeling, which cannot be directly validated due to the lack of Arctic-wide ground truth. The Burke model has been tested before, combined with not only the Vant permittivity formulation, but others too, provides a robust representation of snow-covered sea ice emission at L-band, as has been proved in previous works (Gabarró et al. (2022), Hernández-Macià et al. (2024a), Hernández-Macià et al. (2024b), Hernández-Macià et al. (2025)). The main uncertainty arises from the permittivity, as brine inclusions play a key role and no single formulation has been universally accepted, but this is tackled in this work. Ultimately, the training dataset consists of 199,385,08 pixels extracted from 366 Arctic-wide maps from the model simulations covering two freeze-up seasons (2019–2020 and 2020–2021). After duplicate removal and random shuffling, the dataset was sub-sampled to balance computational cost and performance, resulting in 100,000 unique pixels.

Therefore, this methodology is based in the consecution of two ML inversion steps using RF algorithms: RF-eps (described in Section 4.2), and RF-sit, which is an upgraded version of RF-standard, a previously proposed SMOS-only RF-based method (Hernández-Macià et al., 2024a). In this precursor approach, the sea ice complex permittivity was computed only as a function of its temperature and salinity, following the Vant empirical formulation (Vant et al., 1978). Hereafter, the improved novel methodology algorithm is called RF-synergy (integrating RF-eps and RF-sit), and the RF-standard is kept in the study as a baseline. Figure 6 shows the training and predicting workflows of the RF-sit algorithm. The sea ice conditions are extracted from the same sources as for RF-eps, and are used for both training and predicting. Regarding the permittivity, the training is done using the formulation described in 4.1, and it is then used as an input of the emission model that is inverted to generate the modeled sea ice thickness part of the training dataset. Once the RF-sit algorithm has been trained, the same variables as for RF-standard (Hernández-Macià et al., 2024a) are used alongside the permittivity estimated using RF-eps.

The feature importance analysis highlights differences between the two models. For RF-standard, SMOS TB dominates (94%), with smaller contributions from sea ice temperature (4%), salinity (1%), and snow presence (0.4%). In RF-synergy, which includes the same inputs plus the real and imaginary parts of the complex sea ice permittivity, TB intensity remains the most important (73%), followed by the imaginary part of the the permittivity (26%), while the real part and the thermodynamic

https://doi.org/10.5194/egusphere-2026-422
Preprint. Discussion started: 4 February 2026

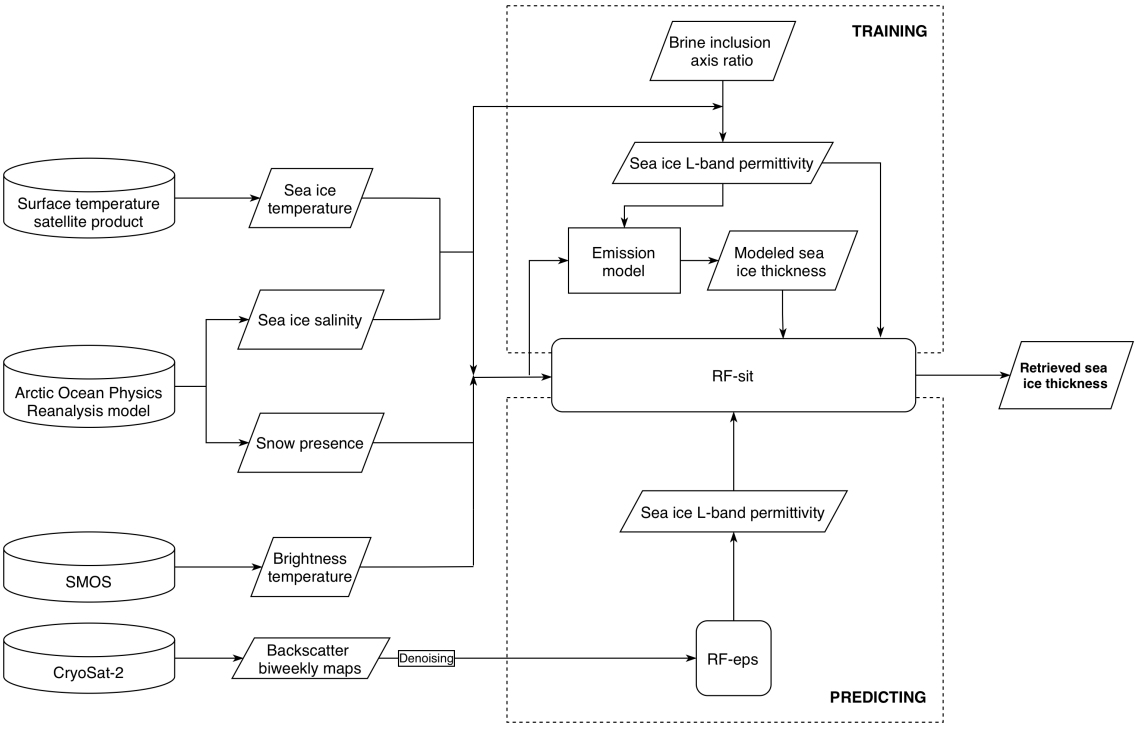

Figure 6. Diagram summarizing the training and predicting workflows of the RF-sit algorithm.

variables contribute marginally (summing 1% among all them). The difference in importance between the real and imaginary parts arises from their distinct variability ranges: the more variable imaginary component (see Figure 4) has a stronger impact on the predictions. Intuitively, when two samples are close in the real-part space, its limited variability reduces its influence, and the imaginary part becomes the dominant factor.

5 Results

The proposed RF-synergy method can be validated using available in situ datasets, and also it can be compared with the AWI/ESA operational product and the previous RF-standard (Hernández-Macià et al., 2024a) method. Although the CS2 data is averaged biweekly, given the daily SMOS coverage, the delivered outputs are daily, allowing the comparison with the other existing SMOS thin SIT products. Figure 7 shows an example of the retrieved SIT from the proposed CS2-SMOS synergy method, RF-synergy, alongside the AWI/ESA and RF-standards baselines, for a particular day (7th of December 2019). It also contains the key variables that are involved in the methodology, i.e. the CS2 backscatter and the SMOS TB, the CS2-estimated permittivity (both real and imaginary parts), and the sea ice temperature and salinity conditions. As shown, both the AWI/ESA and the RF-standard maps are similar, while the pan-Arctic estimation from the RF-synergy present significant differences with them. It presents relevant variance in the thinner sea ice area, but also in the thickest area where no sensitivity is expected

https://doi.org/10.5194/egusphere-2026-422
Preprint. Discussion started: 4 February 2026

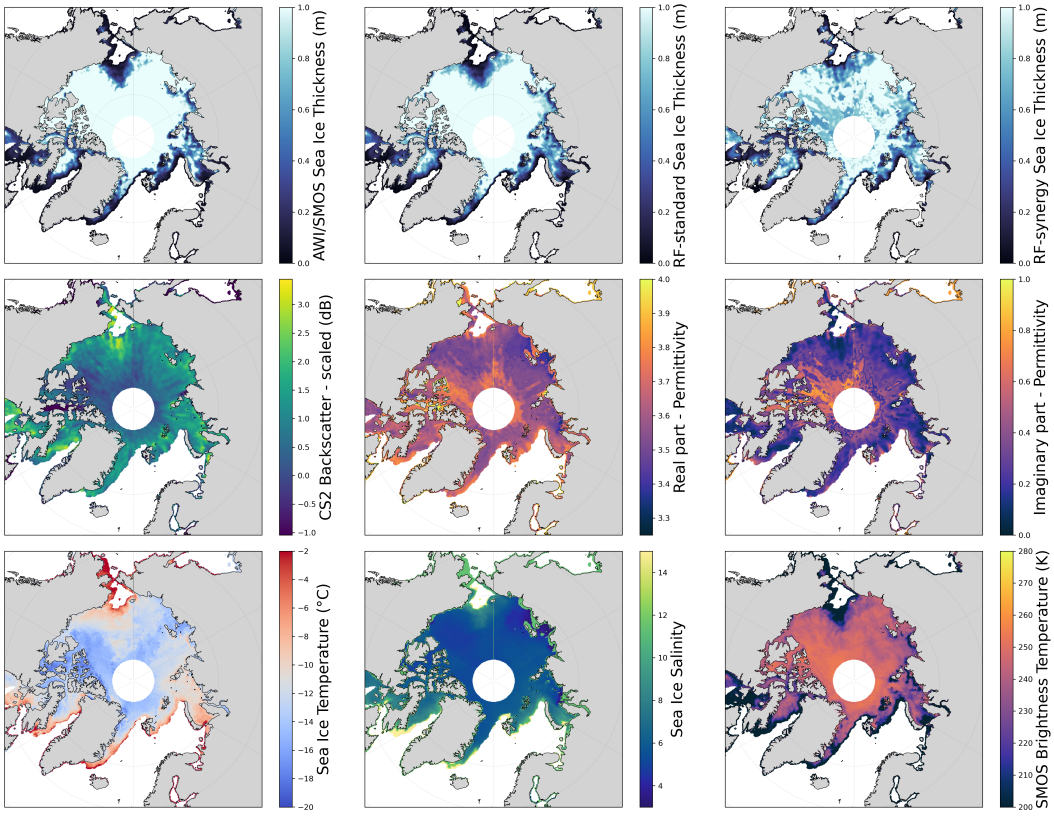

Figure 7. Sea ice thickness from the AWI/ESA operational product (upper-left), the RF-standard method (upper-center) and the synergistic CS2-SMOS approach RF-synergy method (upper-right), alongside the key variables involved in the methodology: CS2 backscatter, estimated real and imaginary parts of the permittivity, sea ice temperature and salinity, and SMOS brightness temperature. Example from the 7th of December 2019.

(Kaleschke et al., 2012). Regarding the CS2 backscatter, which is scaled as detailed in Section 4.2, shows interesting patterns that could be linked to different types of sea ice and thus permittivity variations. The estimated permittivity shows similar behavior as the CS2 backscatter, and it is correlated also with the salinity and specially the temperature. Finally, SMOS TB shows a strong correlation with the different sea ice conditions, thickness (retrieved), temperature and salinity, as expected (Kaleschke et al. (2012), Huntemann et al. (2014)).

Despite the RF-synergy thickness estimations for the particular day that is qualitatively studied are uneven with the other two algorithms, remain crucial to use the sparse but available in situ data to analyze its potential. For this purpose, data from the ESA SMOSice campaign (Kaleschke et al., 2016), from the shipborne SIMS, and from the BGEP moorings is used (see Section 2.5 for furtehr details). Figure 8 shows the estimations from the RF-synergy method alongside the defined baseline products. The validation results are shown separately for each subgroup, HEM, SEM, and ALS, to ease the visualization of

https://doi.org/10.5194/egusphere-2026-422
Preprint. Discussion started: 4 February 2026

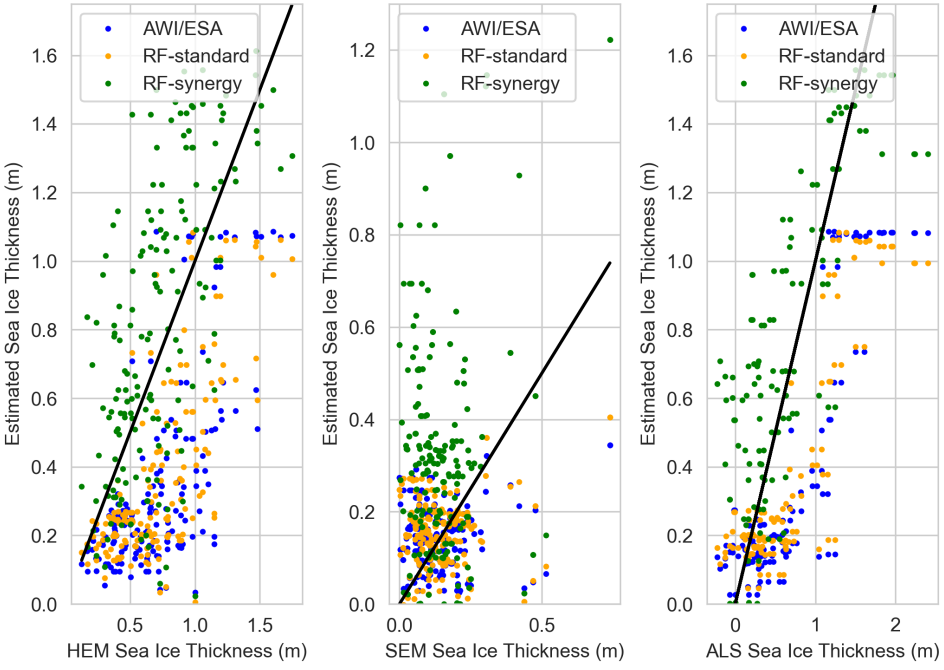

Figure 8. Sea ice thickness estimated with the RF-synergy method alongside the baseline products as a function of the in situ ESA SMOSice campaign measurements (19th to 26th of March 2014).

Metric	AWI/ESA	RF-standard	RF-synergy
HEM			
R^2	0.70	0.73	0.62
MAE (m)	0.39	0.36	0.28
SEM			
R^2	0.10	0.12	0.16
MAE (m)	0.09	0.09	0.24
ALS			
R^2	0.86	0.87	0.79
MAE (m)	0.36	0.35	0.30

Table 1. Metrics for each method for the ESA SMOSice campaign data validation.

https://doi.org/10.5194/egusphere-2026-422
Preprint. Discussion started: 4 February 2026

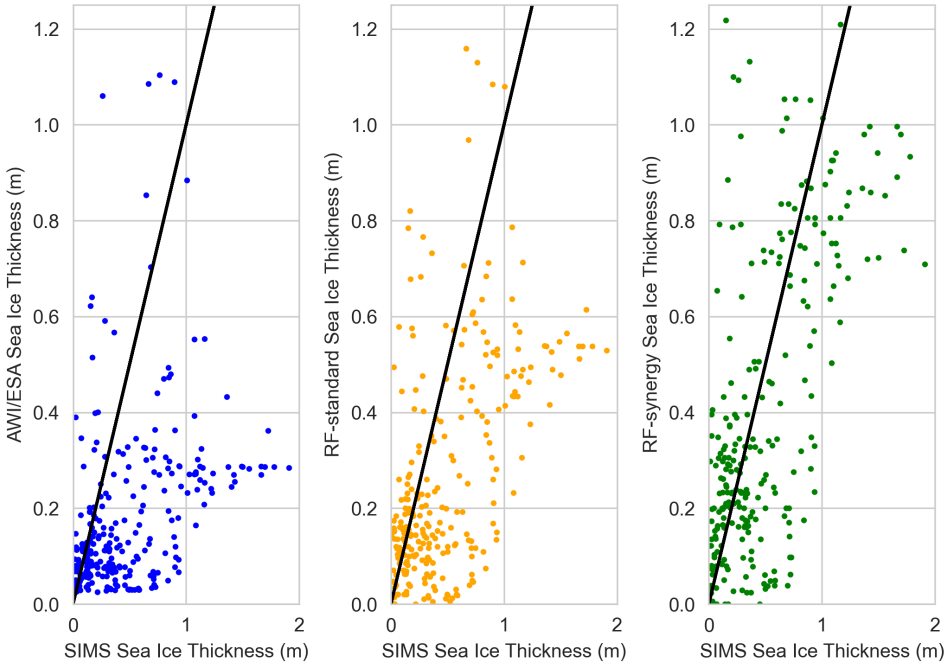

Figure 9. Sea ice thickness estimated with the RF-synergy method alongside the baseline products as a function of the in situ shipborne SIMS measurements in spring 2025 in West Greenland.

Metric	AWI/ESA	RF-standard	RF-synergy
R^2	0.36	0.53	0.63
MAE (m)	0.36	0.31	0.26

Table 2. Metrics for each method for the shipborne SIMS data validation.

their performances. Table 1 presents the metrics for each product, the correlation coefficient (R^2) and the Mean Absolute Error (MAE). In general, the SMOS-only methods, AWI/ESA and RF-standard, have a better correlation but also a higher MAE. This can explain that the RF-synergy seems to be closer to the in situ measurements, thus reducing the error, but also have greater dispersion, leading to the reduced correlation. It is clear that the SEM data is not reproducible by any method, but the HEM and ALS measurements are reasonably well matched, specially with RF-synergy. Specifically for the SEM data, the low MAE mainly reflects the narrow range of the values rather than true predictive skill. In the absence of correlation, the predictions remain numerically close to the targets simply because of the limited dispersion, which artificially lowers the error metric.

A similar analysis can be done with the shipborne SIMS data that was collected in spring (late March, early April) 2025 in West Greenland. Figure 9 shows the estimations from the RF-synergy method along with the baseline products as a function of the SIMS-collected measurements. Table 2 shows the metrics, where in this case not only the correlation is higher for the

https://doi.org/10.5194/egusphere-2026-422
Preprint. Discussion started: 4 February 2026

Metric	AWI/ESA	RF-standard	RF-synergy
BGEP-A			
R^2	0.74	0.79	0.66
MAE (m)	0.39	0.36	0.19
BGEP-B			
R^2	0.66	0.70	0.45
MAE (m)	0.48	0.44	0.21
BGEP-D			
R^2	0.69	0.72	0.53
MAE (m)	0.39	0.37	0.22

Table 3. Metrics for each method for the BGEP moorings data validation.

RF-synergy, but also the MAE is reduced, compared to the SMOS products. In this case, the CS2-SMOS synergistic approach delivers closer estimations to the in situ observations, but also with less dispersion than the baseline methods. Even though the thinner part is covered by all the products, the sensitivity seems to be improved in the thicker part (above 0.6 m) by RF-synergy.

To extend the analysis, the BGEP moorings data can be used to study the sea ice evolution from when it starts growing until when it reaches around 1 m of thickness. This can allow to understand if the integration of the CS2 data to estimate the sea ice permittivity can help in measuring the sea ice temporal evolution and periodicity. Figure 10 shows the SIT temporal evolution estimated by the three methods, versus the BGEP moorings' in situ measurements. The showcased data corresponds to the growth period, from when the SMOS products are available (October 15th onward) until when the ice reaches a thickness of 1 m. Exceptionally, 2013's data is not included because the ice was already too thick (higher than 1 m) at the beginning of the season. Although all the methods are clearly able to follow the temporal evolution, RF-synergy estimations are closer to the in situ observations. However, this matching is far from equal between different years and also between the different moorings, even though they are located in the same area. For instance, 2012 is not reproducible by any method, while for other periods, like 2019, the CS2-SMOS synergy SIT show better agreement. The differences shown in the lower part of Figure 10 confirm that RF-synergy estimations result in an improvement when compared to the in situ observations. In general, the difference is kept below 50 cm, whereas the baseline products are usually over it. Table 3 shows the metrics for each mooring separately. Similarly to what is observed in Table 3, even though the SMOS only products present a higher correlation coefficient, RF-synergy has a significantly reduced (almost 50%) error when compared to the in situ observations.

6 Discussion

To assess the reliability of the permittivity estimated from the CS2 backscatter, it is crucial to understand the physical mechanisms underlying the improvement observed with the RF-synergy method, despite the promising results presented in Section 5. Figure

https://doi.org/10.5194/egusphere-2026-422
Preprint. Discussion started: 4 February 2026

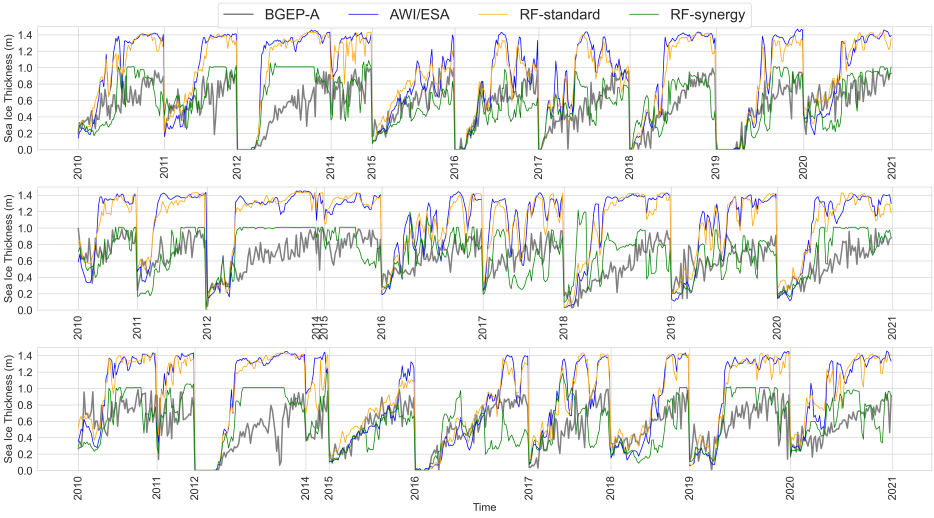

(a) Sea ice thickness estimations from the RF-synergy and the baseline products alongside the in situ BGEP moorings measurements. Each subplot corresponds to each mooring: A, B and D.

(b) Sea ice thickness differences between the RF-synergy and the baseline products with the in situ BGEP moorings measurements. Each subplot corresponds to each mooring: A, B and D.

Figure 10. Sea ice thickness estimations and differences from the RF-synergy and the baseline products with the in situ BGEP moorings measurements. Each subplot corresponds to each mooring: A, B and D. The utilized data is limited to the growth period, until it reached 1 m, for each year between 2010 and 2021, except 2013 where the growth period was too short.

https://doi.org/10.5194/egusphere-2026-422
Preprint. Discussion started: 4 February 2026

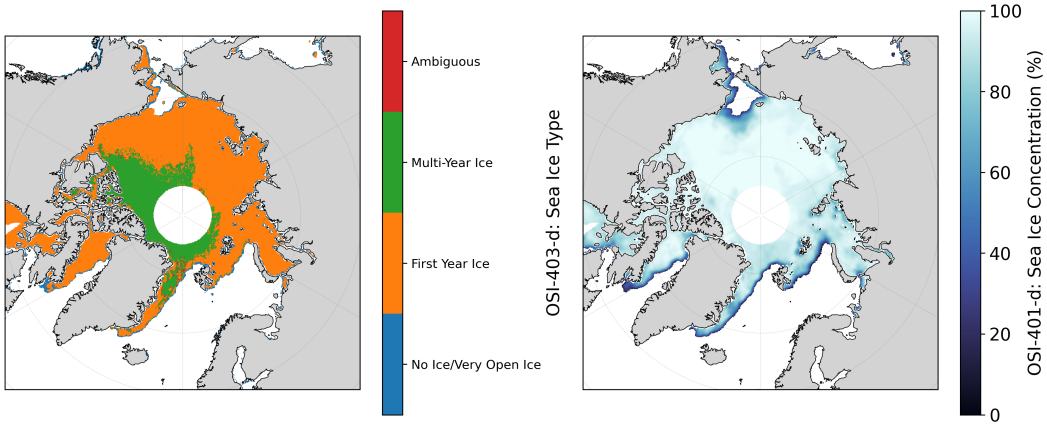

Figure 11. Sea ice type (EUMETSAT OSI SAF OSI-403-d) and sea ice concentration (EUMETSAT OSI SAF OSI-401-b) maps. Example from the 7th of December 2019.

11 shows the sea ice type (EUMETSAT OSI SAF OSI-403-d) and concentration (EUMETSAT OSI SAF OSI-401-d) maps for the same day as Figure 7. As shown, the patterns observed in the CS2 backscatter and the inconsistencies of the RF-synergy SIT estimations mostly match with the multi-year ice (MYI) region. In fact, it is worth mentioning that the SMRT simulations used to train RF-eps and thus RF-synergy, are only considering first-year ice (FYI). This is mainly because the applicability of the L-band radiometry products is limited to thin ice, which in the freeze-up period (October-April) can be assumed to be FYI. Furthermore, the modeling of MYI in the SMRT simulations, as well as in the permittivity model, would require the inclusion of air pockets, in addition to brine inclusions. Therefore, the permittivity estimated with RF-eps can only be considered valid for FYI. This can also be confirmed for what is shown in Figure 7, where both the real and imaginary parts of the permittivity seem to be higher in the MYI than for FYI, which is not realistic (Vant et al. (1978), Ulaby et al. (2014)). For these reasons, to ensure the reliability of the proposed synergistic method, and also considering the patterns observed in Figure 7 in the RF-synergy SIT for the MYI area, its applicability has to be limited to FYI. Regarding the sea ice concentration (SIC) in Figure 11, it presents the expected distribution, with lower concentrations in the marginal ice zone (MIZ), where the ice is growing. There is no apparent relationship with the SIT obtained by RF-synergy, or at least not stronger than that observed with the other products. This suggests that the integration of CS2 backscatter is not solely improving the results by correcting the underestimation associated with the assumption of 100% sea ice concentration in the baseline methods (Tian-Kunze et al. (2014), Hernández-Macià et al. (2024a)). When sea ice concentration is below 100%, the observed inconsistency persists, similarly to what is found in the other approaches.

To further confirm the reliability of RF-synergy, Figures 12 and 13 show scatter plots with the estimated SIT as a function of the in situ measurements for a set of different key variables as colormaps. The analysis has been performed using the following variables: the real and imaginary parts of the permittivity, the (scaled) CS2 backscatter, and the sea ice temperature and salinity conditions. In general, what can be observed is that the thinner ice is related to a higher permittivity (both real and imaginary

https://doi.org/10.5194/egusphere-2026-422
Preprint. Discussion started: 4 February 2026

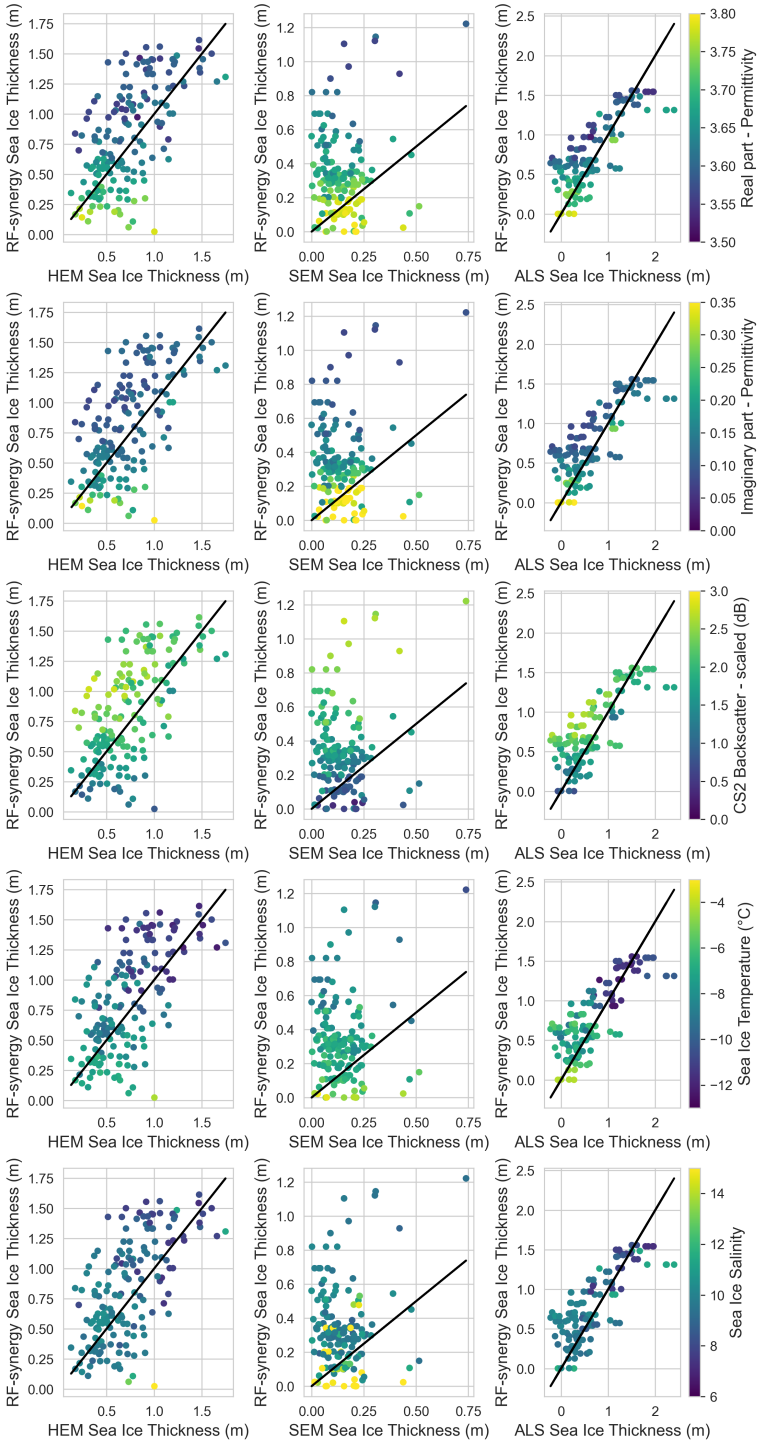

Figure 12. Scatter plots showing the RF-synergy estimations as a function of the ESA SMOSice campaign in situ measurements, with each subplot having a colormap for each key variable identified: the real and imaginary parts of the sea ice permittivity, the CryoSat-2 backscatter, and the sea ice temperature and salinity conditions.

https://doi.org/10.5194/egusphere-2026-422
Preprint. Discussion started: 4 February 2026

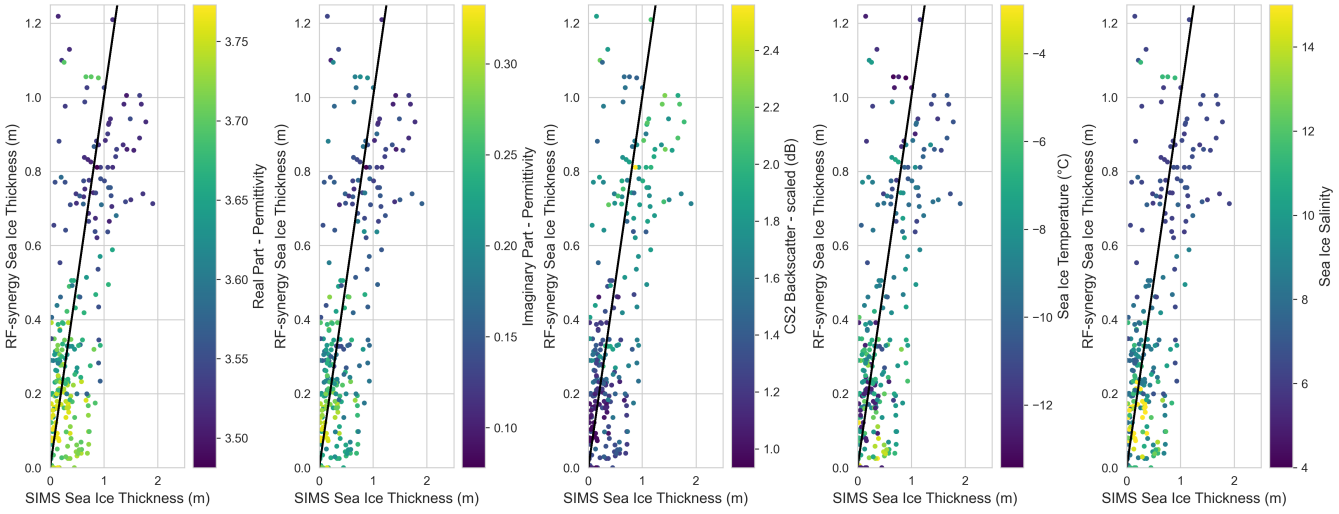

Figure 13. Scatter plots showing the RF-synergy estimations as a function of the shipborne SIMS in situ measurements, with each subplot having a colormap for each key variable identified: the real and imaginary parts of the sea ice permittivity, the CryoSat-2 backscatter, and the sea ice temperature and salinity conditions.

parts). This is realistic as the thinnest ice is the one that is newer and thus is more saline and warmer, and so it has a higher brine volume and so a higher permittivity (Ulaby et al., 2014). This is observed in Figure 12 and 13, as the thinnest ice is indeed related to higher values of temperature and salinity. These findings strongly support the reliability of the proposed CS2-SMOS method, also considering that these links are observed for two independent datasets that differ importantly in time and in space.

Regarding the relationship between Ku-band radar altimetry backscatter and L-band sea ice permittivity, the results demonstrate a statistically robust relationship, as evidenced by the improved retrieval accuracy of RF-synergy. Although an explicit physical formulation has not yet been derived, the correlation proves effective for the proposed retrieval. A systematic discrepancy exists between the SMRT model, which yields negative backscatter values, and the operational CS2 products, which typically report positive values. This difference is attributable to a fixed calibration offset or gain factor applied in the satellite processing chain. However, the dynamic range of the modeled backscatter aligns well with the observations. Since the proposed methodology relies on relative backscatter variations rather than absolute radiometric calibration, this constant offset effectively cancels out and does not impact the validity of the results.

The impact of the roughness in the study is bypassed through the usage of backscatter difference instead of the absolute values. This strategy has been proved to be effective with the accuracy-improved results from RF-synergy. Furthermore, since the CS2 observations integrated in the methodology are interpolated onto the SMOS grid, the roughness variability within the radiometer footprint can be considered to be averaged out, which is also expected to further reduce the influence of this

https://doi.org/10.5194/egusphere-2026-422
Preprint. Discussion started: 4 February 2026

parameter.

Ultimately, to explain the miss-correlation observed in 2012 season in Figure 10, it is important to remark that 2012 was marked by the record-breaking sea ice minimum in September 2012, which created a regime of high instability and exceptionally high sea ice drift velocities. These extreme conditions can affect the ancillary data from reanalysis, i.e. the ocean and sea ice variables used to compute the ice salinity (Section 2.4), leading to biased thickness values. As detailed by Rheinlænder et al. (2022), the ice pack was preconditioned to be thinner and mechanically weaker than usual, making it susceptible to wind-driven fracturing, thus a state that the reanalysis model can struggle to represent.

7 Conclusions

This study has presented a novel synergistic methodology integrating Ku-band radar altimetry backscatter from CryoSat-2 into the SMOS L-band radiometry thin sea ice thickness retrieval algorithm. By addressing the uncertainty regarding sea ice permittivity, the major source of uncertainty in L-band SIT retrievals, the new proposed approach aims to enhance the accuracy of thickness estimates in the Arctic. The permittivity modeling adopted has allowed to simulate this variable under a wide range of different conditions, and to relate it with the Ku-band backscatter using the SMRT model, resulting in a realistic training dataset. The proposed workflow utilizes a two-stage hybrid inversion scheme. First, the *RF-eps* algorithm utilizes CryoSat-2 backscatter to estimate the complex sea ice permittivity. Subsequently, the *RF-sit* algorithm integrates these permittivity estimates within the SMOS SIT retrieval algorithm to retrieve sea ice thickness, resulting in the combined *RF-synergy*.

The performance of the synergistic method has been evaluated against independent in situ datasets and compared to SMOS-only baselines (AWI/ESA and *RF-standard*). This validation demonstrated that the *RF-synergy* method generally yields lower error compared those SMOS-only approaches. Notably, in comparisons with BGEP moorings, the synergistic approach significantly reduced the error, by nearly 50% in some cases, compared to baseline products. Furthermore, the method produced physically consistent results, where thinner ice was associated with higher permittivity values, reflecting the warmer and more saline nature of newly formed ice. Despite these improvements, the analysis of sea ice type maps indicated that the validity of the current method is limited to FYI areas. The training simulations did not account for air pockets characteristic of MYI, leading to unrealistic sea ice permittivity and thickness estimates in those regions. Regarding the theoretical framework, the statistical link between Ku-band backscatter and L-band permittivity derived from SMRT simulations is validated by the improved retrieval performance. Furthermore, the influence of the roughness in the radar altimeter backscatter has been effectively diminished with the CS2 data treatment, i.e. the scaling and the re-projection into to lower-resolution radiometer grid. Ultimately, although an explicit physical formulation is yet to be established and a sign discrepancy exists between modeled and observed backscatter, the consistency in absolute magnitudes and the method's reliance on normalized variations ensure the robustness of the approach.

Overall, this study highlights the potential of cross-sensor synergies to advance thin sea ice monitoring. By effectively combining active Ku-band and passive L-band microwave observations, this method improves the current operational products

https://doi.org/10.5194/egusphere-2026-422
Preprint. Discussion started: 4 February 2026

and offers a robust framework for present and future satellite missions. Beyond the specific configuration of CryoSat-2 and SMOS, this synergistic strategy establishes a paradigm applicable to other frequencies and sensor combinations, paving the way for upcoming missions such as CIMR, CRISTAL or ROSE-L. Crucially, this work demonstrates that establishing synergy at a fundamental level, by utilizing active sensor observations to constrain the physical parameters driving the passive retrieval, rather than merely merging independent thickness products, presents a high-potential pathway for the next generation of polar observing systems.

Code and data availability. The source codes are available for downloading at the following link: https://github.com/ferranhema/altimetry-radiometry-synergy-sit. The production of the AWI/ESA SMOS sea ice thickness data was supported by the ESA project 'SMOS & CryoSat-2 Sea Ice Data Product Processing and Dissemination Service,' and the data are available at https://smos-diss.eo.esa.int. The processing of the RF-standard data was carried out at the Barcelona Expert Center on Remote Sensing (BEC-RS, https://bec.icm.csic.es) of the Institut de Ciències del Mar (ICM-CSIC), and it is available at https://doi.org/10.20350/digitalCSIC/17749 and will also be accessible via the center's FTP service. The RF-synergy dataset generated in this study is available upon request. The BGEP data used for validation were collected and made available by the Beaufort Gyre Exploration Project based at the Woods Hole Oceanographic Institution (https://www2.whoi.edu/site/beaufortgyre), in collaboration with researchers from Fisheries and Oceans Canada at the Institute of Ocean Sciences.

Author contributions. Conceptualization, F.H.-M., M.J.E., C.G., G.S.G. and A.G.-M.; methodology, F.H.-M., M.J.E., C.G., G.S.G. and A.G.-M.; software, F.H.-M.; validation, F.H.-M.; formal analysis, F.H.-M.; investigation, F.H.-M.; resources, F.H.-M., M.J.E., C.G., G.S.G. and A.G.-M.; data curation, F.H.-M.; writing—original draft preparation, F.H.-M.; writing—review and editing, M.J.E., C.G., G.S.G. and A.G.-M.; visualization, F.H.-M.; supervision, M.J.E., C.G., G.S.G. and A.G.-M.; project administration, C.G. and M.J.E.; funding acquisition, C.G. and M.J.E. All authors have read and agreed to the published version of the manuscript.

Competing interests. No competing interests are present.

Acknowledgements. This project is funded with the ARCTIC-MON project (PID2021-125324OB-I00) from the Agencia Estatal de Investigación in Spain and is supported by the Spanish government through the 'Severo Ochoa Centre of Excellence' accreditation (CEX2024-001494-S) to ICM-CSIC. Remote sensing data processing has been executed at the Barcelona Expert Center on Remote Sensing (BEC-RS, https://bec.icm.csic.es) of the Institut de Ciències del Mar ICM-CSIC. This work has been conducted in the framework of the PhD in Computer Science program of the Universitat Autònoma de Barcelona (UAB). This work is part of a Doctorat Industrial (AGAUR), with expedient number 2023 DI 0007. We acknowledge PONANT and the crew of Le Commandant Charcot for the ship time and technical support, allowing to collect the SIMS dataset used in the study.

https://doi.org/10.5194/egusphere-2026-422
Preprint. Discussion started: 4 February 2026

References

Assur, A.: Composition of sea ice and its tensile strength, Tech. rep., Technical report, U.S. Army Snow, Ice and Permafrost Research Establishment, Wilmette, Ill, 1960.

Beaven, S. G., Lockhart, G. L., Gogineni, S. P., Hosseinmostafa, A. R., Jezek, K., Gow, A. J., Perovich, D. K., Fung, A. K., and Tjuatja, S.: Laboratory measurements of radar backscatter from bare and snow-covered saline ice sheets, International Journal of Remote Sensing, 16, 851–876, 1995.

Belter, H. J., Krumpen, T., Hendricks, S., Hoelemann, J., Janout, M. A., Ricker, R., and Haas, C.: Satellite-based sea ice thickness changes in the Laptev Sea from 2002 to 2017: comparison to mooring observations, The Cryosphere, 14, 2189–2203, https://doi.org/10.5194/tc-14-2189-2020, 2020.

Burke, W., Schmugge, T., and Paris, J.: Comparison of 2.8- and 21-cm microwave radiometer observations over soils with emission model calculations, Journal of Geophysical Research, 84, 287–294, https://doi.org/https://doi.org/10.1029/JC084iC01p00287, 1979.

Copernicus Marine Service (CMEMS): Arctic Ocean - Sea and Ice Surface Temperature REPROCESSED, Copernicus Marine Service (CMEMS), https://doi.org/10.48670/moi-00123, 2024a.

Copernicus Marine Service (CMEMS): Arctic Ocean Physics Reanalysis, Copernicus Marine Service (CMEMS), https://doi.org/10.48670/moi-00007, 2024b.

Dawson, G. J. and Landy, J. C.: Comparing elevation and backscatter retrievals from CryoSat-2 and ICESat-2 over Arctic summer sea ice, The Cryosphere, 17, 4165–4178, https://doi.org/10.5194/tc-17-4165-2023, publisher: Copernicus GmbH, 2023.

Dinardo, S.: Guidelines for reverting Waveform Power to Sigma Nought for CryoSat-2 in SAR mode, Technical Note XCRY-GSEG-EOPS-TN-14-0012, European Space Agency (ESA), issue 2, Revision 2, 2016.

Donlon, C., Galeazzi, C., Midthassel, R., Sallusti, M., Triggianese, M., Fiorelli, B., De Paris, G., Kornienko, A., and Khlystova, I.: The Copernicus Imaging Microwave Radiometer (CIMR): Mission Overview and Status, in: IGARSS 2023 - 2023 IEEE International Geoscience and Remote Sensing Symposium, pp. 989–992, https://doi.org/10.1109/IGARSS52108.2023.10281934, 2023.

Doronin, Y.: Thermal interaction of the atmosphere and the hydrosphere in the Arctic, CoronetBooks, Philadelphia, 1971.

Entekhabi, D., Njoku, E. G., O'Neill, P. E., Kellogg, K. H., Crow, W. T., Edelstein, W. N., Entin, J. K., Goodman, S. D., Jackson, T. J., Johnson, J., Kimball, J., Piepmeier, J. R., Koster, R. D., Martin, N., McDonald, K. C., Moghaddam, M., Moran, S., Reichle, R., Shi, J. C., Spencer, M. W., Thurman, S. W., Tsang, L., and Van Zyl, J.: The Soil Moisture Active Passive (SMAP) mission, Proceedings of the IEEE, 98 (5), 704–716, 2010.

ESA: CryoSat-2 Product Handbook, European Space Agency, https://earth.esa.int/eogateway/documents/20142/0/CryoSat-Product-Handbook-Baseline-E-draft.pdf, baseline E, 2021.

Fetterer, F. M., Drinkwater, M. R., Jezek, K. C., Laxon, S. W. C., Onstott, R. G., and Ulander, L. M. H.: Sea ice altimetry, in: Microwave Remote Sensing of Sea Ice, edited by Carsey, F. D., vol. 68 of *Geophysical Monograph Series*, pp. 111–135, American Geophysical Union, Washington, D.C., USA, https://doi.org/10.1029/GM068, 1992.

Frankenstein, G. and Garner, R.: Equations for Determining the Brine Volume of Sea Ice from -0.5° to -22.9°C., Journal of Glaciology, 6, 943–944, https://doi.org/10.3189/S0022143000020244, 1967.

Gabarró, C., Fabregat, P., Hernández-Macià, F., Jove, R., Salvador, J., Spreen, G., Thielke, L., Dadic, R., Huntemann, M., Kolabutin, N., Nomura, D., Hannula, H.-R., and Schneebeli, M.: First results of the ARIEL L-band radiometer on the MOSAiC Arctic Expedition during

https://doi.org/10.5194/egusphere-2026-422
Preprint. Discussion started: 4 February 2026

the late summer and autumn period, Elementa: Science of the Anthropocene, 10, https://doi.org/10.1525/elementa.2022.00031, 00031, 2022.

Grenfell, T., Barber, D., Fung, A., Gow, A., Jezek, K., Knapp, E., Nghiem, S., Onstott, R., Perovich, D., Roesler, C., Swift, C., and Tanis, F.: Evolution of electromagnetic signatures of sea ice from initial formation to the establishment of thick first-year ice, IEEE Transactions on Geoscience and Remote Sensing, 36, 1642–1654, https://doi.org/10.1109/36.718636, 1998.

Hernández-Macià, F., Gabarró, C., Gomez, G. S., and Escorihuela, M. J.: A Machine Learning Approach on SMOS Thin Sea Ice Thickness Retrieval, IEEE Journal of Selected Topics in Applied Earth Observations and Remote Sensing, 17, 10 752–10 758, https://doi.org/10.1109/JSTARS.2024.3406921, 2024a.

Hernández-Macià, F., Gabarró, C., Huntemann, M., Naderpour, R., Johnson, J. T., and Jezek, K. C.: On sea ice emission modeling for MOSAiC's L-band radiometric measurements, Annals of Glaciology, p. 1–14, https://doi.org/10.1017/aog.2024.38, 2024b.

Hernández-Macià, F., Sanjuan Gomez, G., Gabarró, C., and Escorihuela, M. J.: Assessment of Machine Learning-Driven Retrievals of Arctic Sea Ice Thickness from L-Band Radiometry Remote Sensing, Computers, 14, https://doi.org/10.3390/computers14080305, 2025.

Huntemann, M.: Thickness retrieval and emissivity modeling of thin sea ice at L-band for SMOS satellite observations, Ph.D. thesis, University of Bremen, 2015.

Huntemann, M., Heygster, G., Kaleschke, L., Krumpen, T., Mäkynen, M., and Drusch, M.: Empirical sea ice thickness retrieval during the freeze-up period from SMOS high incident angle observations, The Cryosphere, 8, 439–451, https://doi.org/10.5194/tc-8-439-2014, 2014.

Jones, S. B. and Friedman, S. P.: Particle shape effects on the effective permittivity of anisotropic or isotropic media consisting of aligned or randomly oriented ellipsoidal particles, Water Resources Research, 36, 2821–2833, https://doi.org/https://doi.org/10.1029/2000WR900198, 2000.

Kaleschke, L., Tian-Kunze, X., Maaß, N., Mäkynen, M., and Drusch, M.: Sea ice thickness retrieval from SMOS brightness temperatures during the Arctic freeze-up period, Geophysical Research Letters, doi:10.1029/2012GL050916, 2012.

Kaleschke, L., Tian-Kunze, X., Maaß, N., Beitsch, A., Wernecke, A., Miernecki, M., Müller, G., Fock, B. H., Gierisch, A. M., Schlünzen, K. H., Pohlmann, T., Dobrynin, M., Hendricks, S., Asseng, J., Gerdes, R., Jochmann, P., Reimer, N., Holfort, J., Melsheimer, C., Heygster, G., Spreen, G., Gerland, S., King, J., Skou, N., Søbjærg, S. S., Haas, C., Richter, F., and Casal, T.: SMOS sea ice product: Operational application and validation in the Barents Sea marginal ice zone, Remote Sensing of Environment, 180, 264–273, https://doi.org/https://doi.org/10.1016/j.rse.2016.03.009, special Issue: ESA's Soil Moisture and Ocean Salinity Mission - Achievements and Applications, 2016.

Kerr, Y., Waldteufel, P., Wigneron, J.-P., Martinuzzi, J., Font, J., and Berger, M.: Soil moisture retrieval from space: the Soil Moisture and Ocean Salinity (SMOS) mission, IEEE Transactions on Geoscience and Remote Sensing, 39, 1729–1735, https://doi.org/10.1109/36.942551, 2001.

Kerr, Y., Waldteufel, P., Wigneron, J., Delwart, S., Cabot, F., Boutin, J., Escorihuela, M., Font, J., Reul, N., Gruhier, C., Juglea, S., Drinkwater, M., Hahne, A., Martin-Neira, M., and Mecklenburg, S.: The SMOS mission: New tool for monitoring key elements of the global water cycle, Proceedings of the IEEE IGARSS 2010, no. 5., 98, 666–687, 2010.

Kovacs, A., RESEARCH, C. R., NH., E. L. H., of Engineers, U. S. A. C., Research, C. R., and (U.S.), E. L.: Sea Ice: Bulk salinity versus ice floe thickness, no. part 1 in CRREL report, U.S. Army Cold Regions Research and Engineering Laboratory, https://books.google.es/books?id=DYXZAQAACAAJ, 1996.

https://doi.org/10.5194/egusphere-2026-422
Preprint. Discussion started: 4 February 2026

Landy, J. C., Petty, A. A., Tsamados, M., and Stroeve, J. C.: Sea Ice Roughness Overlooked as a Key Source of Uncertainty in CryoSat-2 Ice Freeboard Retrievals, Journal of Geophysical Research: Oceans, 125, e2019JC015 820, https://doi.org/10.1029/2019JC015820, publisher: John Wiley & Sons, Ltd, 2020.

Larue, F., Picard, G., Aublanc, J., Arnaud, L., Robledano-Perez, A., Le Meur, E., Favier, V., Jourdain, B., Savarino, J., and Thibaut, P.: Radar altimeter waveform simulations in Antarctica with the Snow Microwave Radiative Transfer Model (SMRT), Remote Sensing of Environment, 263, 112 534, https://doi.org/10.1016/j.rse.2021.112534, publisher: Elsevier BV, 2021.

Laxon, S. W., Giles, K. A., Ridout, A. L., Wingham, D. J., Willatt, R., Cullen, R., Kwok, R., Schweiger, A., Zhang, J., Haas, C., Hendricks, S., Krishfield, R., Kurtz, N., Farrell, S., and Davidson, M.: CryoSat-2 estimates of Arctic sea ice thickness and volume, Geophysical Research Letters, 40, 732–737, https://doi.org/https://doi.org/10.1002/grl.50193, 2013.

Maass, N., Kaleschke, L., Tian-Kunze, X., and Tonboe, R. T.: Snow thickness retrieval from L-band brightness temperatures: a model comparison, Annals of Glaciology, 56, 9–17, https://doi.org/10.3189/2015AoG69A886, 2015.

Mallett, R. D. C., Stroeve, J. C., Tsamados, M., Landy, J. C., Willatt, R., Nandan, V., and Liston, G. E.: Faster decline and higher variability in the sea ice thickness of the marginal Arctic seas when accounting for dynamic snow cover, The Cryosphere, 15, 2429–2450, 2021.

Mangilli, A., Duguay, C. R., Murfitt, J., Moreau, T., Amraoui, S., Mugunthan, J. S., Thibaut, P., and Donlon, C.: Improving the Estimation of Lake Ice Thickness with High-Resolution Radar Altimetry Data, Remote Sensing, 16, 2510, https://doi.org/10.3390/rs16142510, number: 14 Publisher: Multidisciplinary Digital Publishing Institute, 2024.

Markus, T., Neumann, T., Martino, A., Abdalati, W., Brunt, K., Csatho, B., Farrell, S., Fricker, H., Gardner, A., Harding, D., et al.: The Ice, Cloud, and land Elevation Satellite-2 (ICESat-2): Science requirements, concept, and implementation, Remote Sensing of Environment, 190, 260–273, 2017.

Meredith, M., Sommerkorn, M., Cassotta, S., Derksen, C., Ekaykin, A., Hollowed, A., Kofinas, G., Mackintosh, A., Melbourne-Thomas, J., Muelbert, M., Ottersen, G., Pritchard, H., and Schuur, E.: Polar Regions. In: IPCC Special Report on the Ocean and Cryosphere in a Changing Climate, Cambridge University Press, Cambridge, UK and New York, NY, USA, pp. 203–320, https://doi.org/https://doi.org/10.1017/9781009157964.005, 2019.

Rheinlænder, J. W., Davy, R., Ólason, E., Rampal, P., Spensberger, C., Williams, T. D., et al.: Driving mechanisms of an extreme winter sea ice breakup event in the Beaufort Sea, Geophysical Research Letters, 49, e2022GL099 024, https://doi.org/10.1029/2022GL099024, 2022.

Ricker, R., Hendricks, S., Kaleschke, L., Tian-Kunze, X., King, J., and Haas, C.: A weekly Arctic sea-ice thickness data record from merged CryoSat-2 and SMOS satellite data, The Cryosphere, 11, 1607–1623, https://doi.org/10.5194/tc-11-1607-2017, 2017.

Ryvlin, A. I.: Method of forecasting flexural strength of an ice cover, Probl. Arct. Antarct., p. 79–86, 1974.

Shokr, M.: Field observations and model calculations of dielectric properties of Arctic sea ice in the microwave C-band, IEEE Transactions on Geoscience and Remote Sensing, 36, 463–478, https://doi.org/10.1109/36.662730, 1998.

Tian-Kunze, X., Kaleschke, L., Maaß, N., Mäkynen, M., Serra, N., Drusch, M., and Krumpen, T.: SMOS-derived thin sea ice thickness: algorithm baseline, product specifications and initial verification, The Cryosphere, 8, 997–1018, https://doi.org/10.5194/tc-8-997-2014, 2014.

Tomasi, C. and Manduchi, R.: Bilateral filtering for gray and color images, in: Sixth International Conference on Computer Vision (IEEE Cat. No.98CH36271), pp. 839–846, https://doi.org/10.1109/ICCV.1998.710815, 1998.

Tonboe, R. T.: Radar backscatter modelling for sea ice radar altimetry, Tech. Rep. DMI Report 17–17, Danish Meteorological Institute, https://www.dmi.dk/fileadmin/user_upload/Rapporter/TR/2017/DMIRep17-17_rtt.pdf, 2017.

https://doi.org/10.5194/egusphere-2026-422
Preprint. Discussion started: 4 February 2026

Ulaby, F., Long, D., and of Michigan. Press, U.: Microwave Radar and Radiometric Remote Sensing, University of Michigan Press, ISBN 9780472119356, 2014.

Vant, M., Ramseier, R., and Makios, V.: The complex-dielectric constant of sea ice at frequencies in the range 0.1–40 GHz, Journal of Applied Physics, 49, 1264–1280, 1978.

Vinje, T. and Finnekåsa, Ø.: The Ice Transport Through the Fram Strait, Norsk Polarinstitutt Oslo: Skrifter, Norsk Polarinstitutt, ISBN 9788290307443, 1986.

von Abedyll, L., J. K. F. v. B. u. P. and Haas, C.: Sea ice thickness, ice loads, and navigability during the North Pole cruise CC110823 of Le Commandant Charcot in August 2023, Tech. rep., Alfred Wegener Institute, Helmholtz Centre for Polar and Marine Research, Bremerhaven, Germany, 2024.

Warren, S. G., Rigor, I. G., Untersteiner, N., Radionov, V. F., Bryazgin, N. N., Aleksandrov, Y. I., and Colony, R.: Snow Depth on Arctic Sea Ice, Journal of Climate, 12, 1814–1829, https://doi.org/10.1175/1520-0442(1999)012<1814:SDOASI>2.0.CO;2, 1999.

Wessel, P., Luis, J. F., Uieda, L., Scharroo, R., Wobbe, F., Smith, W. H. F., and Tian, D.: The Generic Mapping Tools Version 6, Geochemistry, Geophysics, Geosystems, 20, 5556–5564, https://doi.org/https://doi.org/10.1029/2019GC008515, 2019.

Wingham, D., Rapley, C., and D, G.: New Techniques in Satellite Altimeter Tracking Systems, 1986.